JOURNAL OF MATERIALS SCIENCE: 30 (1995) 2901–2910

Metastable liquid phase separation in tungsten inert gas and electron beam copper/stainless-steel welds

A. MUNITZ
Nuclear Research Center–Negev, P.O. Box 9001 Beer-Sheva, Israel

The microstructure of Tungsten Inert Gas (TIG) and electron beam copper/stainless-steel welds were investigated using scanning electron microscopy. The relatively high cooling rates entailed in the welding result in high bulk supercooling, causing two microstructural effects: (i) melt separation into two liquids, iron-rich L1, and copper-poor L2, while each solidifies by a path dictated by the stable phase boundary; (ii) enhanced solute trapping of Cu in the α-Fe phase, and Fe in the ε-Cu phase.

1. Introduction

The bonding between stainless steel and copper has many industrial applications such as in heat exchangers and safes, where the unique properties of the two materials are required, e.g. the heat conductivity of copper and the corrosion resistance of stainless steel. The welding of such dissimilar metals containing large amounts of Fe and Cu usually depends on various factors. The high thermal conductivity of the copper poses a problem in the welding due to dissipation of most of the heat input, particularly during TIG welding. This problem is less important in electron beam welding, as this technique is capable of providing higher power densities. Since the major constituents are Fe and Cu, no intermetallic compounds are expected to form in the welds. The low mutual miscibility between Fe and Cu makes it possible to weld such a pair using Tungsten Inert Gas (TIG) or electron beam welding (EB) techniques. In the present work we investigated the effect of the heating power on the weld microstructure between stainless steel and copper tubes using TIG and electron beam welding.

Another factor that might improve the bonding between the stainless steel tube and the copper tube is the occurrence of melt separation during welding. In previous studies we have found [1–2] that solidification of Fe–Cu alloys at high cooling rates, such as resolidification of electron beam melted surfaces [1] and molten pockets in explosively bonded Fe–Cu plates [2], induces dynamic bulk melt supercooling. Occurrence of melt separation depends on the alloy composition and the level of supercooling, as well as on the solution thermodynamics. For example, systems like Cu–Fe and Cu–Co exhibit a definite thermodynamic tendency to liquid immiscibility upon supercooling, as evident by the nearly flat liquidus curves and the positive deviation of their activities from a Raoultian behaviour [3]. Indeed, it was found that when Cu–Fe alloys are supercooled below a certain temperature, T_{SEP}, which depends on its composition, the liquid metal enters a metastable liquid miscibility gap, and separates into two liquids: an iron-rich melt (L1), and a copper-rich melt (L2), as illustrated in the binary Cu–Fe phase diagram in Fig. 1. Each melt then solidifies on a path dictated by the stable phase diagram boundary. Usually, high supercooling levels might be obtained in pure materials, where reduced numbers of heterogeneous nucleation sites are expected. Therefore, it would be of great value to know whether separation into two liquids occurs in welding commercial copper and stainless-steel pipes as well.

2. Experimental procedure

Copper and stainless-steel tubes of 4 cm outer diameter and 5 mm wall thickness were welded by Tungsten Inert Gas (TIG) or by an Electron Beam (EB). For TIG welding the surfaces were prepared to have v-shaped grooves. The tubes were pre-heated and then welded using 130–140 A d.c. current and 20–30 V with the stainless-steel filling electrode (Inconel type 82). For electron beam welding the surfaces were prepared with square edges. The welding conditions were the following: velocity 9.2 RPM (100 cm/min), voltage 60 kV, current 22 mA. The electron beam was focused on the tube's surface.

Samples containing the welds were cut into rectangles, and used for scanning electron microscopy. The samples were prepared by standard metallographic techniques, with a final polish using 0.25 μm fine diamond paste as the abrasive and Kerosene as the lubricant. After polishing, the specimens were further etched using either of the following etchants: (i) 2 ml HNO_3 in 100 ml methanol (Nital) at room temperature, for 5 seconds, (ii) 120 ml H_2O, 10 g.

0022–2461

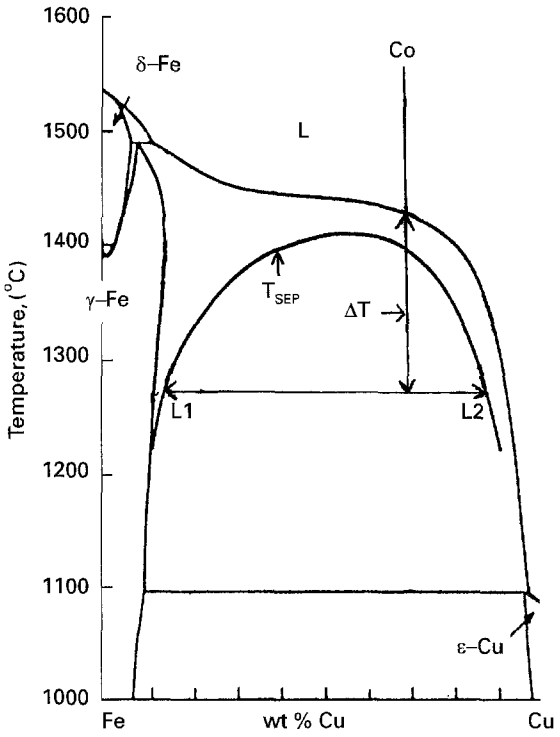

Figure 1 A Cu–Fe phase diagram demonstrating the separation of a liquid with C_0 composition into two liquids: Fe-rich L1, and Cu-rich L2.

ammonium cupric chloride and ammonium hydroxide of weight sufficient to dissolve all the ammonium cupric chloride crystals. The room-temperature etching time ranged between 5 and 12 seconds. The microstructure and compositional profiles were investigated using a scanning electron microscope (SEM–Phillips type 505 with energy dispersive spectroscopy capabilities (EDS)). For the EDS analysis, the specimens were etched only lightly, enough to reveal the microstructure yet keep the surface roughness to a minimum. The data were corrected with a standard ZAF computer program [4].

3. Results and discussion

3.1. TIG welding of copper/stainless-steel tubes

In Figs 2 to 4 we present secondary electron images illustrating the TIG welding microstructure of copper/stainless-steel tubes. The macrostructure of the resolidified molten pool of Cu/stainless-steel welds is complicated, as illustrated in Fig. 2 and in the schematic drawing in Fig. 3. As will be discussed later, the reason for the large differences in the microstructures emerges from two main sources. (i) The large differences in heat conductivities, and the heat absorption capabilities of the two materials composing the matrix, which induce different cooling rates at different parts in the molten pool. This in turn causes diverse paths of solidification such as melt separation and microstructural refinement. (ii) During welding of the copper tube, the stainless-steel tube and the filling

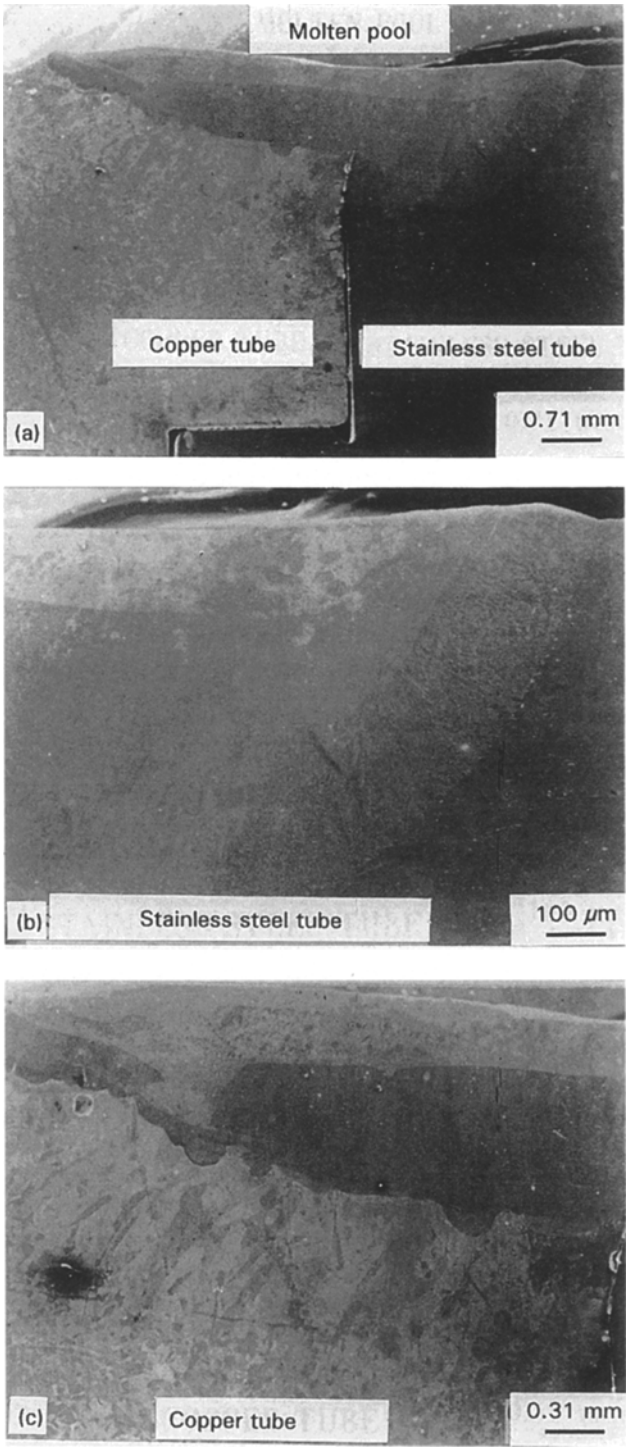

Figure 2 Secondary electron images demonstrating the microstructure of a TIG weld of copper and stainless-steel tubes. (a) An overall view, (b) stainless-steel side at higher magnification, (c) copper side at higher magnification.

electrode melt. The short resolidification time does not allow full homogenization. Therefore, differences in composition in different parts of the fused zone are expected. Convection might cause solutal bands due to spreading of the original melted material in the molten pool along its moving trail (we shall see that this phenomenon is emphasized in EB welding). Therefore, if solidification time is short, it could induce some solute inhomogeneity in the microscale. As can be seen from Fig. 2a, and in the enlargements

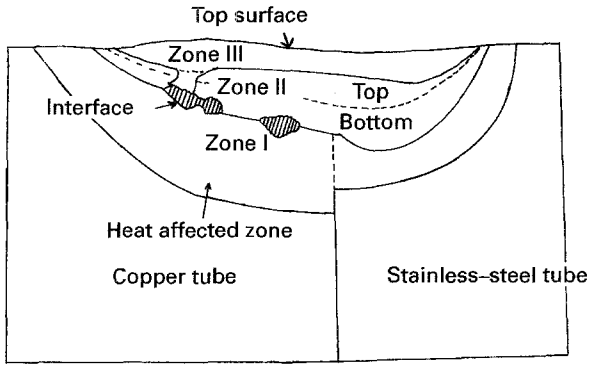

Figure 3 Schematic illustration of the different zones in a TIG weld of copper and stainless-steel tubes.

of the stainless-steel and copper sides in Fig. 2b and c, respectively, the fused zone contains 3 different microstructural zones: (i) a bottom layer near the fusion line – Zone I, which we identify as the heat affected zone (HAZ). The heat absorption in the copper substrate is larger than the heat absorption in the stainless steel. Therefore, the HAZ on the copper side is broader than on the stainless-steel side; (ii) a centre layer – Zone II, and (iii) a top layer – Zone III. To clarify the macrostructure, a schematic illustration is provided in Fig. 3. The microstructure of the welds above the copper tube and above the stainless-steel tube are given in Figs 4 and 5, respectively.

3.1.1. The microstructure of the copper side

The microstructure of the copper side of the fused zone is demonstrated in Fig. 4. The region near the fusion line, Zone I, consisted of large columnar grains; see the lower part of Fig. 4a. X-ray microanalysis indicates that the grains near the fusion line contain copper, with a total of 1 wt % Fe, Cr and Ni. It is reasonable to assume that this zone has recrystallized in the solid state without actually melting (heat affected zone (HAZ)). The enhanced Fe, Cr and Ni concentrations are due to diffusion. The microstructure of the intermediate layer, which exists at the fusion line between the recrystallized copper grains and Zone II (Fig. 3), is illustrated in the middle layer in Fig. 4b, and by a higher magnification in Fig. 4c and d. The average Cu concentration is only 23 wt %, as detailed in Table I.

The microstructure of Zone II consisted of two layers: (i) a bottom layer exhibiting a smooth dendritic morphology, and an interdendritic filling phase at the bottom of Zone II, see Fig. 4e; (ii) the top layer of Zone II. The compositions of the different phases found in the seams of the TIG welds are summarized in Table 1. While the bottom structure of Zone II consisted of the regular dendritic microstructure, the microstructure of the top layer of Zone II was irregular. In the top layer of Zone II one observes a spherical morphology (bright sphere in Fig. 4f) which contains 76.4 wt % Cu and 15.1 wt % Fe embedded in a smooth matrix containing 22.9 wt % Cu and 53.9 wt % Fe (as we shall discuss later, only the ratio between the Cu and Fe content is important. The absolute composition are given in Table I). The X-ray spectrum of the top layer of Zone II, and the spectrum of the sphere with its surrounding matrix, is given on the right-hand side of Fig. 4f. The density of the L2 spheres increases on approaching Zone III. The microstructure of Zone III is presented in Fig. 4g and h. The matrix contains 53.1 wt % Cu and 29.1 wt % Fe. In Fig. 4g and h one observes almost the same morphology as for the top layer of the second zone, i.e. spheres embedded in a matrix. Here, however, the sphere contains 22.1 wt % Cu and 54.2 wt % Fe, while the matrix contains 79.6 wt % Cu and 12.7 wt % Fe. X-ray composition spectra of the sphere and the matrix are indicated on the right-hand side of Fig. 4h. The white particles inside the L1 spheres contain larger amounts of Cu, but due to their small dimensions, the exact composition could not be resolved.

Since a Fe–Cr–Ni–Cu phase diagram is lacking, we shall discuss the results on the basis of our experience with the Cu–Fe phase diagram (Fig. 1) and on some preliminary results we have on melting the same Cu and stainless steel tubes by arc (details are being prepared for publication separately [5]). For alloys of Fe–Cr–Ni–Cu containing 90 to 65 wt % Cu which solidify at low cooling rates, the first phase to solidify will be an α-Fe phase, which contains about 12 wt % Cu (and 18 wt % Cr, 7.1 wt % Ni and 63.0 wt % Fe). At a certain temperature a peritectic reaction will take place, in which some of the primary α-Fe phase reacts with the remaining liquid to form an ε-Cu phase. As the peritectic reaction continues, the ε-Cu grows around the α-Fe dendrites until the latter are completely surrounded. Then, the peritectic reaction slows down drastically due to the limited solid-state diffusion. The remaining liquid solidifies as an ε-Cu phase. The ε-Cu phase contains 87.5 wt % Cu, 1.8 wt % Cr, 3.1 wt % Ni and 7.6 wt % Fe.

The microstructure of the fused zone depends on the supercooling obtained during solidification. Usually, when resolidification starts, the thermal gradient at the fusion line, G, is very large, while the interface velocity, R, is very small. Thus G/R is large. According to the classical constitutional supercooling criterion [6], conditions for plane front solidification thus exist, and a plane front growth takes place. In our case no indication of plane front solidification was observed; presumably the width of this zone is smaller than the resolution limit. As solidification proceeds, the thermal gradients decrease and the interface velocities increase. Thus, G/R decreases markedly. The factor G/R becomes smaller, and solidification changes into dendritic, as can be seen in Figs 4e and 5c. At the same time, as proposed in some of our previous publications [1, 7, 8], considerable dynamic supercooling could take place due to the large heat transport as compared to the mass transport. This in turn might cause melt separation. The appearance of spherulites of one composition in a matrix of another composition implies that liquid phase separation occurred prior to solidification [1]. As soon as the liquid enters the miscibility gap it separates into two liquids, a Fe-rich one (L1) and a Cu-rich one (L2) (as in the case of

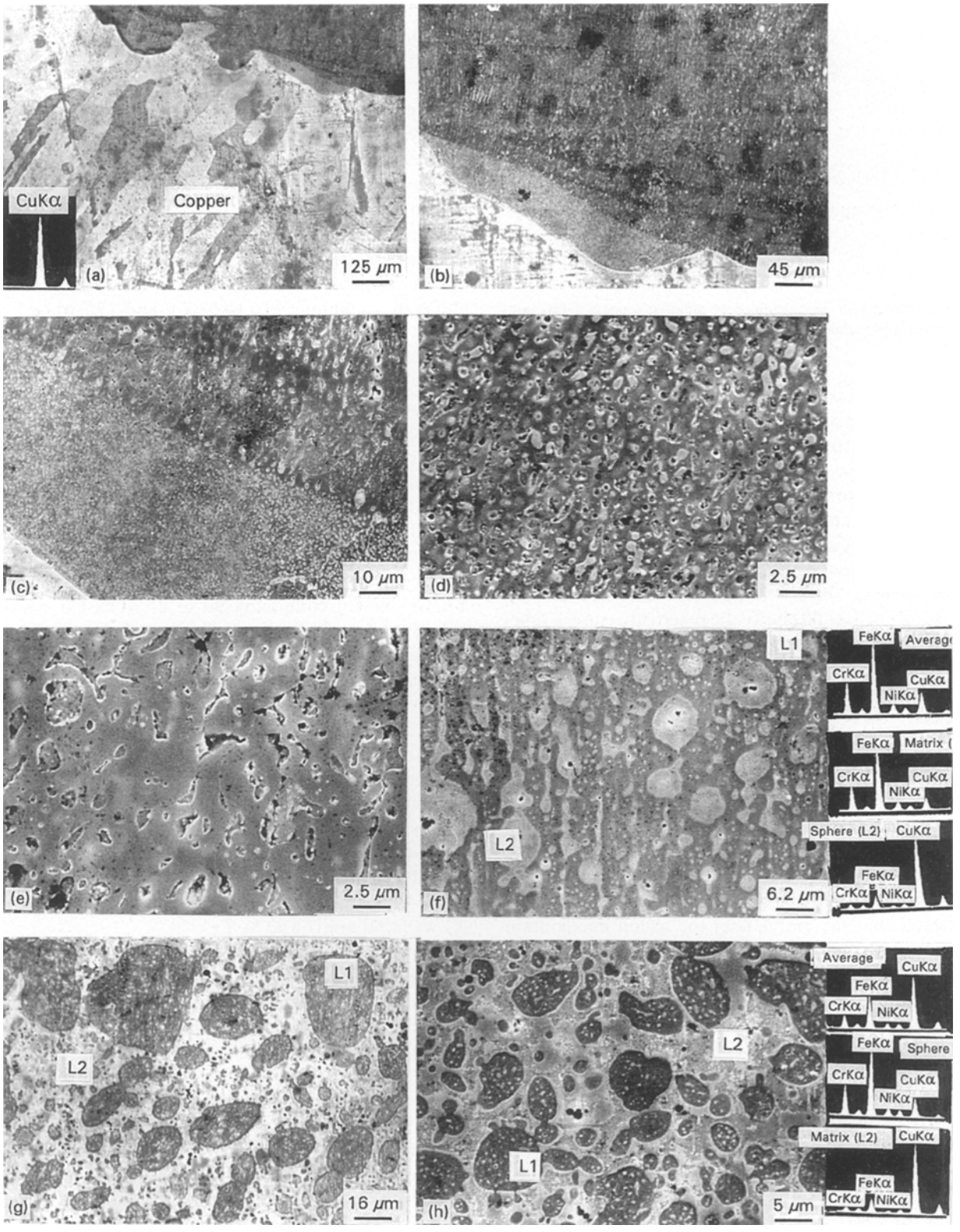

Figure 4 Secondary electron images illustrating the microstucture of a TIG weld of copper and stainless-steel tubes at the copper side at higher magnification. (a) Heat afftcted zone, (b–d) interfac of copper-matrix/zone I at different magnifications; (e) bottom layer of Zone II; (f) top layer of Zone II. X-ray spectr of the average composition, the sphere and the matrix are indicated on the right-hand side of Fig. 3h, (g–h) Zone III. X-ray spectra of the average composition, the sphere and the matrix are indicated on the right-hand side of Fig. 3h.

Figure 5 Secondary electron images demonstrating the microstructure of a TIG weld of copper and stainless-steel welded tubes at the stainless-steel side at higher magnification. X-ray spectra of relevant compositions are indicated on the right-hand side of Fig. 4b, d, f, and h. (a) Heat affected zone. (b) interface of stainless-steel matrix/Zone I; (c–d) microstructure of Zone I; (e) the microstructure of Zone II; (f) enlargement of L2 sphere, (g–h) microstructure of Zone III, (i, j) the microstructure of the very top surface.

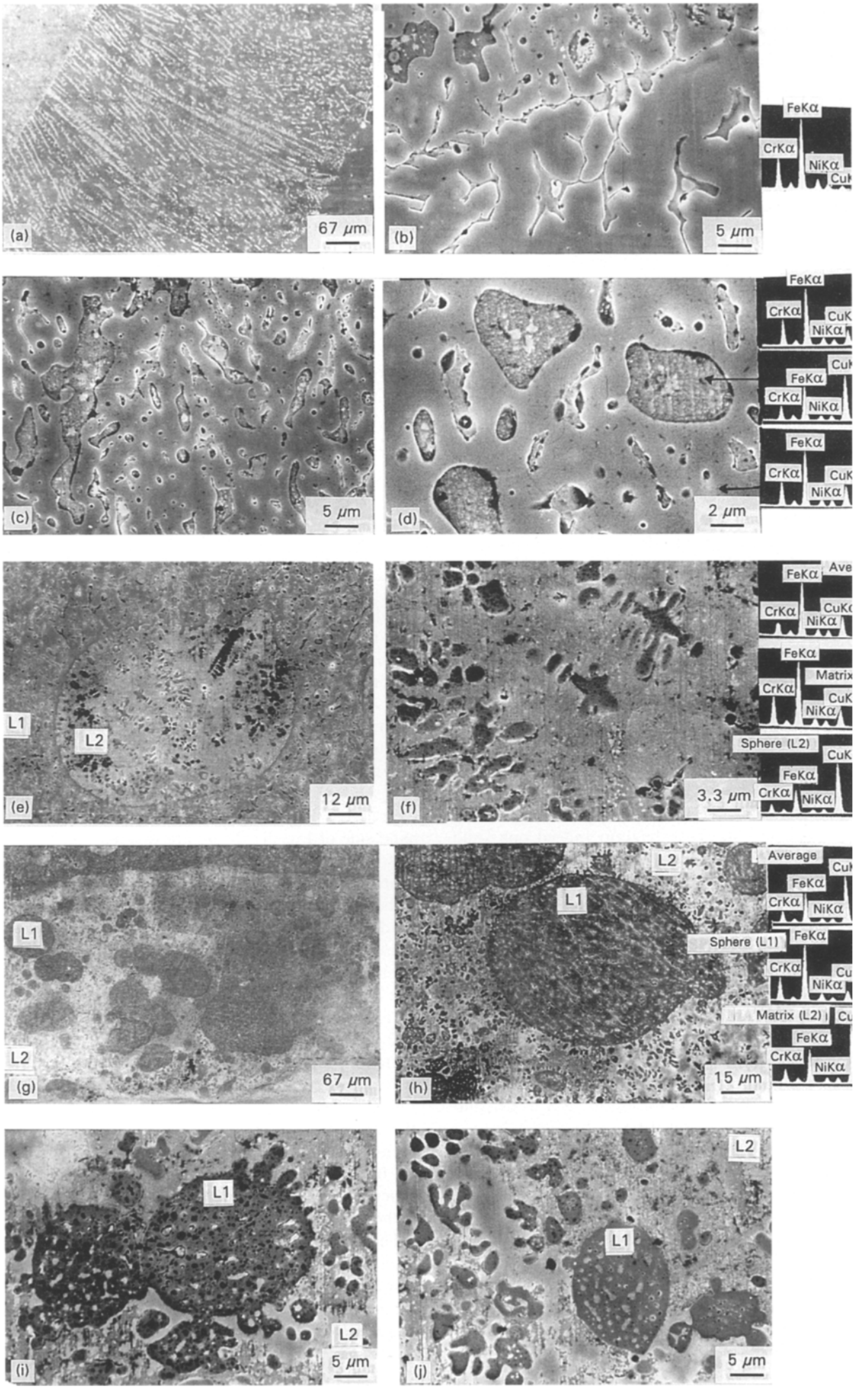
(a)
67 μm
(b)
5 μm
FeKα
CrKα
NiKα
(c)
5 μm
(d)
2 μm
(e)
L1
L2
12 μm
(f)
3.3 μm
Sphere (L2)
Matrix
Ave
(g)
L1
L2
67 μm
(h)
L1
L2
15 μm
Average
Sphere (L1)
Matrix (L2)
(i)
L1
L2
5 μm
(j)
L1
L2
5 μm

TABLE I Summary of compositional analysis of the different phases of TIG welded copper/stainless-steel tubes

	Region investigated		Cr wt %	Fe wt %	Ni wt %	Cu wt %
	Average stainless-steel		20.9	70.2	8.9	0.0
	Average interface Cu matrix/zone I		16.9	52.5	7.2	23.4
		Average	19.4	61.2	7.1	11.5
	Zone II	Dendrite	19.9	63.0	7.2	9.8
	Bottom layer	Interdendritic	2.6	7.9	3.8	85.7
Copper side		Average	8.8	48.3	6.3	29.3
	Zone II	L1-Matrix	16.4	63.9	6.9	22.9
	Top layer	L2-Sphere	4.7	15.1	3.9	76.4
		Average	9.4	29.1	4.9	53.1
	Zone III	L1-Sphere	16.4	54.2	7.3	22.1
		L2-Matrix	4.5	12.7	3.1	79.6
	Surface (above Zone III)	Average	6.4	20.5	4.5	68.5
	HAZ-Zone I		20.8	70.3	8.9	0.0
		Average	15.8	42.8	6.5	28.0
	Zone II	Dendrite	19.9	63.1	7.1	9.8
	Bottom layer	Interdendritic	3.1	8.6	3.2	85.2
		Average	15.4	47.5	6.4	30.6
Stainless steel side	Zone II	L1-Matrix	16.2	54.4	7.3	22.1
	Top layer	L2-Sphere	4.9	15.1	3.9	76.4
		Fe Dendrite in L2	11.6	47.2	9.3	31.9
		Average	10.4	31.7	5.4	52.4
	Zone III	L1-Sphere	15.7	51.5	7.0	25.2
		L2-Matrix	4.4	12.8	3.1	79.6

the binary Cu–Fe system of Fig. 1). For example, as can be seen in Table I, when a liquid containing 48.3 wt % Fe, 8.8 wt % Cr, 6.3 wt % Ni and 29.3 wt % Cu enters the miscibility gap, it will separate into two different liquids, a Fe-rich liquid, L1, which contains 53.9 wt % Fe, 16.4 wt % Cr, 6.9 wt % Ni and 22.9 wt % Cu, and a Cu-rich liquid, L2, which contain 15.1 wt % Fe, 4.7 wt % Cr, 3.9 wt % Ni and 76.4 wt % Cu. Both liquids solidify simultaneously, one in the form of spheres and the other as the matrix, depending on the system stable phase diagram. Indeed, one could observe Cu-rich particles inside the L1 spheres (Fig. 4h). As we shall see in the next section, one could observe α-Fe dendrites inside the L2 structure (Fig. 5f). The quantities of the L1 and L2 liquids follow the lever rule at the metastable miscibility gap boundaries. The spheres (or matrix) may originate from L1 or L2 liquids. If the liquid contains less than 50 wt % Cu, the spheres originate from the L2 liquid as for Zone I (Fig. 4f). If the average liquid contains more than 50 wt % Cu the spheres originate from L1, as for Zone III (Fig. 4g and h). A similar phenomenon was observed in the solidification of Cu–Co and Cu–Fe supercooled liquids [3, 8].

3.1.2. The microstructure of the fused zone above the stainless-steel matrix

As described earlier, the microstructure of the fused zone above the stainless-steel matrix consists of three zones. The microstructure of the first zone is presented in Fig. 5a. The composition of this zone is almost the same as that of the matrix. This indicates that it is a heat affected zone (HAZ). The second zone (II) consisted of two layers as on the copper side; the microstructures of the bottom and top layers are presented in Fig. 5c and d, and Fig. 5e and f, respectively. The microstructure of the bottom layer of Zone II consists of dendrites containing large amounts of Fe dendrites, and Cu-rich interdendritic phases. The average composition of the bottom layer, the interdendritic composition and the dendrite composition spectra are indicated on the right-hand side of Fig. 5d. The microstructure of the top layer consisted of Cu-rich spheres embedded in a Fe-rich matrix (compare the relative peaks in the X-ray spectra on the right-hand side of Fig. 5f). There are two main differences between Zone II above the stainless steel or above the copper: (a) The amount of the interdendritic phase is higher above the stainless steel, since the interdendritic phase contains a large copper concentration (compare Figs 4e and 5d). (b) The spheres on the top layer are bigger, their density is larger, and a substructure may be observed inside the sphere, as can be seen in Fig. 5f. The dark dendrite in Fig. 5f contains 47.2 wt % Fe and 31.9 wt % Cu embedded in a matrix containing only 15.1 wt % Fe and 76.4 wt % Cu. In spite of the fact that both layers in the same zone have almost the same composition (around 47 wt % Fe and 30 wt % Cu), the microstructure is completely different. Regular dendritic solidification could be seen at the bottom layer, while at the top layer the microstructure is characteristic of an alloy which solidified in the miscibility gap.

The microstructure of Zone III also exhibits liquid phase separation (Figs 5g through 5j). However, since the average alloy composition in this region is larger than 50 wt % Cu, the spheres consisted of the L1 liquid instead of L2 spheres, as evinced by the X-ray spectra on the right side of Fig. 5h. The bright phase in the sphere contains large amounts of Cu.

An important feature of rapid cooling, such as those obtained during TIG welding, is the possibility of achieving melt supercooling [7, 8]. At slow cooling rates, the evolution of heat of fusion compensates for the heat removal, and the melt freezes close to its equilibrium freezing point. At cooling rates which exist during the TIG welding, the heat removal rate exceeds the heat of fusion releasing rate. The melt thus supercools. It has been argued [7–9] that under rapid cooling conditions, a supercooled liquid may continue to supercool even in the presence of solid nuclei. This is a result of competition between the cooling and the nuclei growth rates. The heat flow takes place predominantly through the solid. The matrix acts as a natural nucleus. Therefore, the first materials solidify very close to the melting temperature. As solidification proceeds, both the solid and the liquid temperatures decrease below the liquidus temperature due to the high rate of heat extraction. The supercooling near the solidifying front is higher than the centre of the molten pool. Vigorous convections are associated with TIG welding. These convections produce an almost homogeneously supercooled liquid in the entire molten pool. Therefore, the top layer, which stays longer in the liquid state, might exhibit larger dynamic bulk supercooling.

3.2. Electron beam welding of copper/stainless-steel tubes

In Figs 6 to 8 we present, at different magnifications, secondary electron images illustrating the macro- and microstructures of electron beam welds of copper and stainless-steel tubes. In Fig. 6 a general view of the weld top and middle macrostructures at different magnifications is presented. Due to the high power density of the electron beam, full penetration is obtained with a narrow heat affected zone. The black stripes at the middle of the penetration depth which extend from the top to the bottom of Fig. 6c are indicative of the severe melt convections which exist during electron beam welding. Antony and Cline [10] suggested that temperature gradients which are involved during the melting process generate large melt motions. This liquid, when solidified on the recommencement of growth, generates the solute banding, which in turn causes microstructural differences (different colours on etching). The microstructure of the welds is a function of the location in the weld. Generally, there are three different regions: (i) the top region, ranging down from the top surface to about 250 μm, (ii) the region between 250 μm to about 2 mm from the top surface, and (iii) the remaining regions. The microstructures of the different regions are presented in Fig. 7. The microstructure at the weld top is presented in Fig. 7a and b. It consists of spheres embedded in a featureless matrix. X-ray microanalysis of the spheres and matrix indicates that they contain 57.5 and 7.7 wt % Fe, respectively, and 21.2 and 88.4 wt % Cu, respectively. The average melt composition contains 24.0 wt % Fe and 65.9 wt % Cu. The measured compositions of the different phases are given in Table II. Such microstructures and compositions

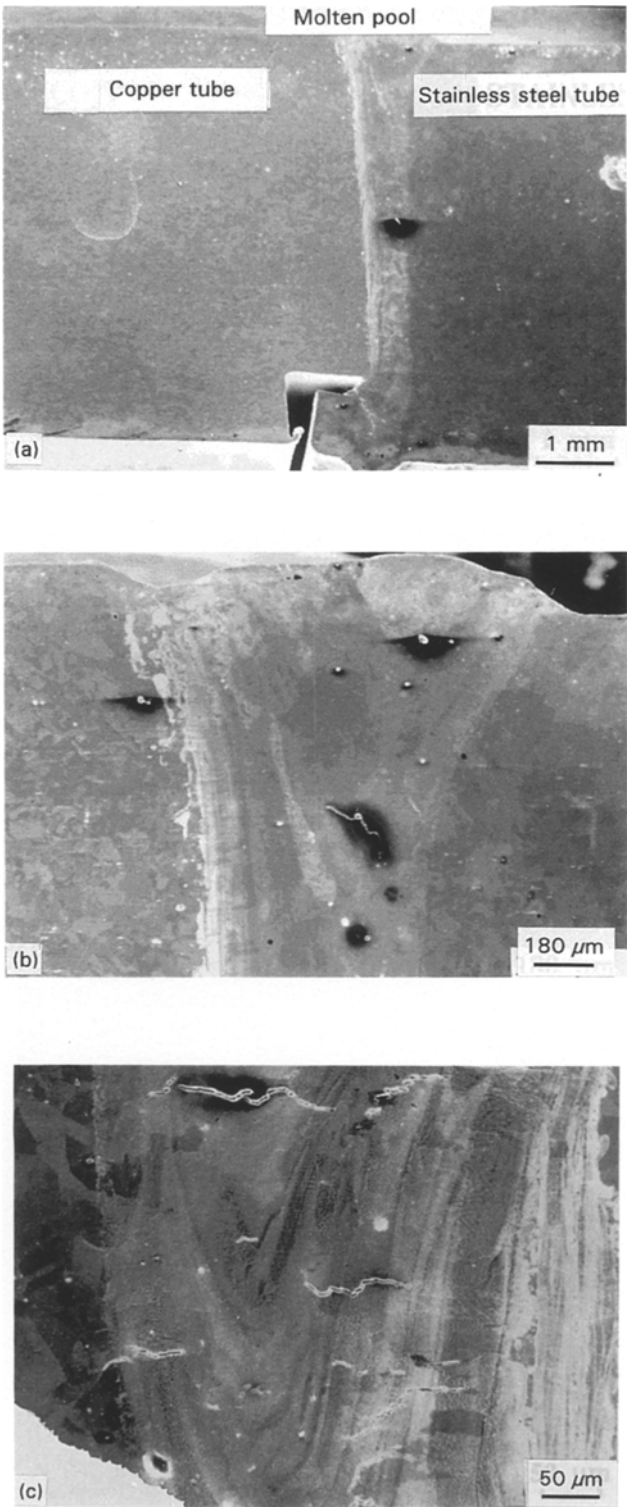

Figure 6 Secondary electron images illustrating the macrosture of an electron beam weld of copper and stainless-steel tubes at three magnifications.

are characteristic of liquid phase separation. There are, however, two main differences between the microstructures of the electron beam welds and the TIG welds: (1) finer microstructure which resulted from the higher cooling rates occurring during solidification; (2) existence of secondary liquid phase separation. This results from the high cooling rates causing large dynamic bulk supercooling in the liquid even after separation. As the liquid is cooled within the miscibility gap, the compositions of the two

TABLE II Summary of compositional analysis of the different phases observed in electron beam welds of copper/stainless-steel tubes

Zone	Region investigated		Cr wt %	Fe wt %	Ni wt %	Cu wt %
Top layer	1st region	Average	7.1	24.0	3.1	65.9
		L1-sphere	16.2	57.5	5.3	21.2
		L2-matrix without spheres	2.0	7.7	1.9	88.4
		L2-matrix including spheres	5.5	19.6	3.0	71.9
	2nd region	Average	12.7	44.3	5.6	37.5
		L1-matrix	14.6	50.2	6.3	28.7
		L2-spheres	2.6	7.6	2.3	87.5
Bottom weld		Average	16.9	60.0	7.3	15.8

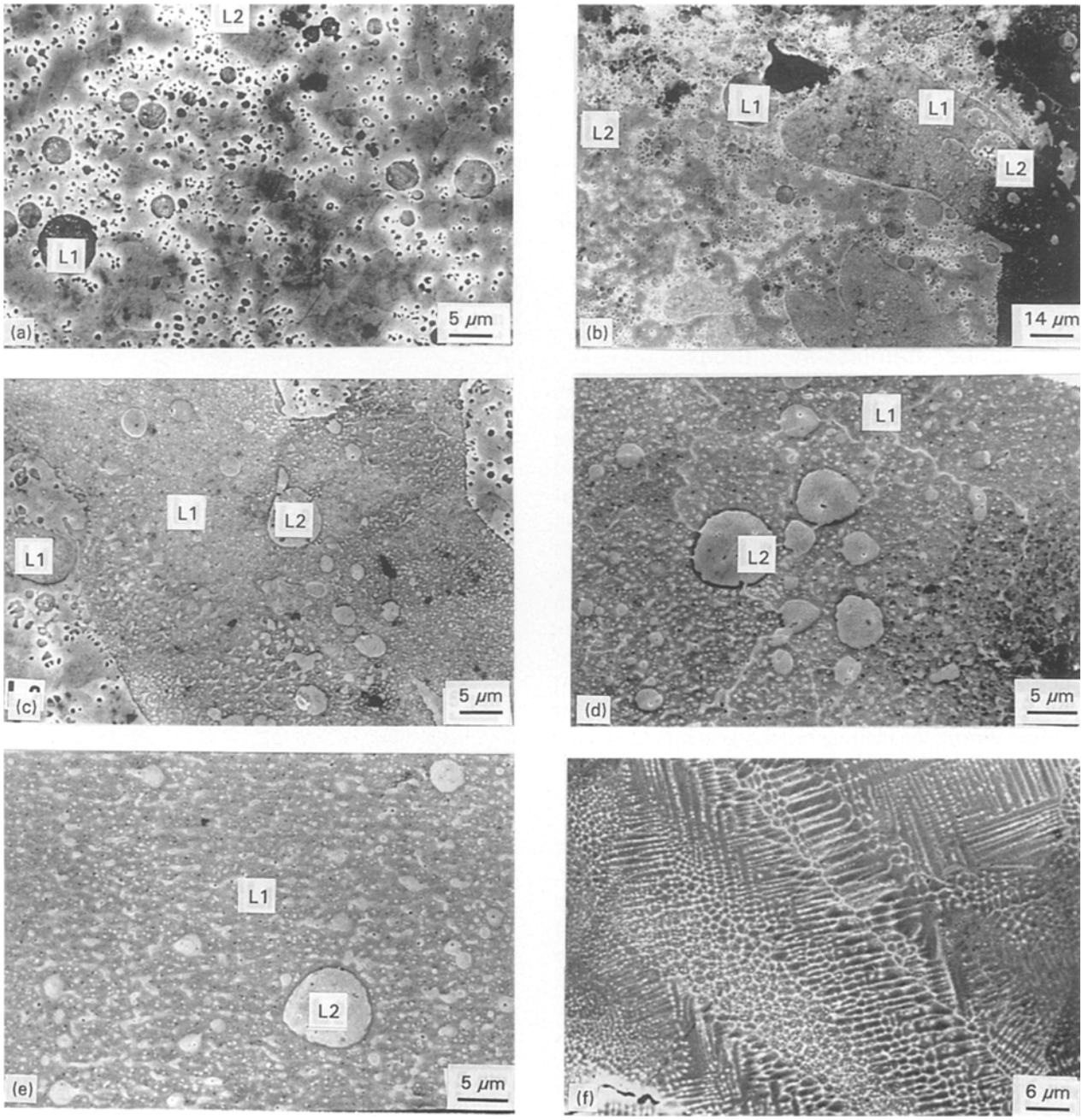

Figure 7 Secondary electron images demonstrating the microstructure of an electron beam weld of copper and stainless-steel tubes at different locations.

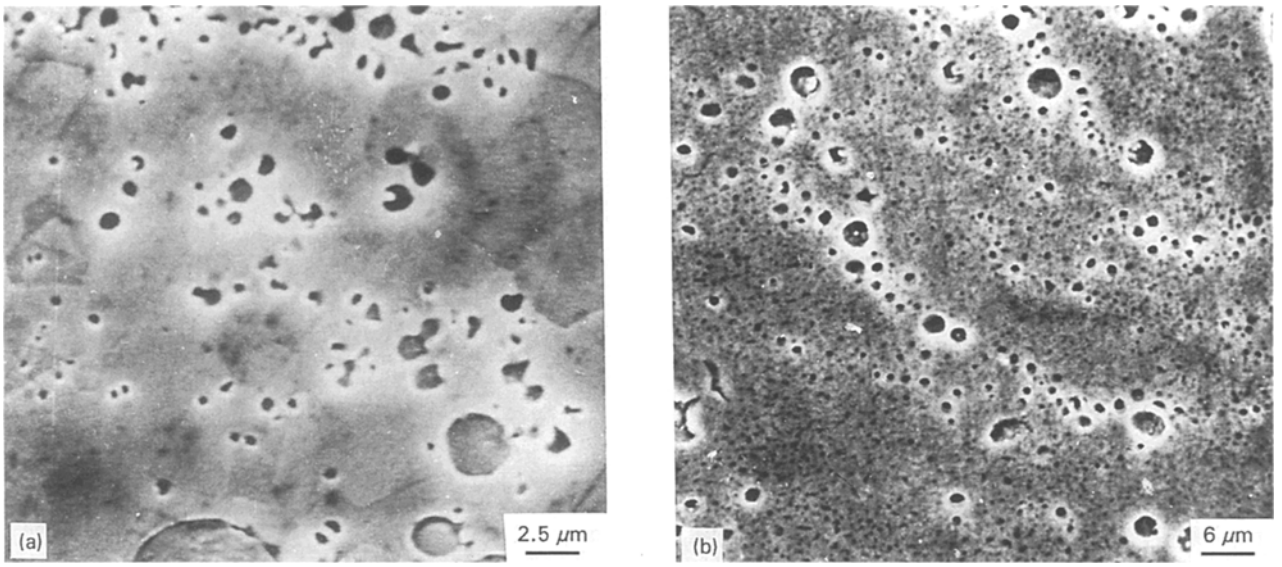

Figure 8 Secondary electron images demonstrating the microstructure of Cu-rich phase (L2 melt) for two different etchants. (a) Etchant ii of Section 2, (b) Nital.

phase-separated liquids attempt to follow the limits of the immiscibility boundaries by diffusion. In the absence of complete diffusion, and as the temperature decreases, secondary phase separation may take place as a result of supersaturation of one or both of the primary separated phases. The amount of super saturation which can be obtained depends on the cooling rate within the miscibility gap, the rate of diffusion, and the shape of the miscibility gap. The cooling rates involved during EB welding are higher than during TIG welding. Therefore, secondary melt separation could be observed in the fused zone in EB welds, as evinced in Fig. 7b. In the middle of the right side of Fig. 7b one observes the L1 region in which secondary L2 parts precipitate. Furthermore, inside the L2 parts one observes dark spheres of L1 composition. A similar phenomenon has been well documented in glasses [11–13] where the melt has been cooled stepwise in the miscibility gap. In liquid metals the viscosity is lower and diffusion is faster; therefore, less time is needed to adjust the composition of the primary separated phases.

The microstructure of the second region (at about 0.5 mm below the top) consisted of Cu-rich L2 spheres embedded in a Fe-rich matrix, as illustrated in Fig. 7b and c. The density of the L2 spheres decreased with depth below the outer surface. At about 1.8 mm from the top surface (Fig. 7e) very few L2 spheres could be revealed. Below 2 mm from the top surface (region iii) the matrix contains only 15.8 wt % Cu with a regular dendritic structure (Fig. 7f) without any spheres.

To get a better understanding of the microstructural details of the internal microstructure of the L2 phase, several samples were also etched with Nital (an etchant used to expose Fe parts). In Fig. 8 the microstructure of the top layer (region (i)) is presented for two types of etchant: the regular etchant (etchant ii of Section 2) to expose copper-rich phases (Fig. 8a) and Nital (Fig. 8b) to expose Fe-rich ones. The dark fine particles revealed inside the featureless matrix in Fig. 7b imply enhanced solute trapping (Fe atoms) in the Cu structure during solidification. Upon cooling to room temperature the iron atoms become immiscible in the Cu structure, and thus precipitates. Due to the high cooling rates involved during solidification of the electron beam seams, high bulk supercooling would be expected [1, 2]. At least 150 K supercooling was obtained during the resolidification of electron beam surface-melted Cu – 10 wt % Co [8]. High bulk supercooling causes high solidification velocities, which in turn might increase the effective distribution coefficient, resulting in enhanced Fe solubility in the Cu structure. In the extreme case of very high solidification velocity, the effective distribution coefficient approaches unity. Then, effectively a partitionless solidification (i.e., complete solute trapping) occurs.

3.3. The spherulite size dependence on convection conditions

The process of melt separation is quite complex. As the liquid is supercooled into the miscibility gap, the melt separates into two liquids. At the onset of separation, under our experimental conditions, submicrometre L1 droplets nucleate and grow in the L2 melt. While the alloy is supercooled within the miscibility gap these small isolated droplets coarsen and/or grow in a spherical shape, minimizing the surface energy. Also, these particles may impinge on each other and coalesce due to the large convection in the molten pool. If the kinetic energy of the colliding droplets is lower than the energy needed for the surface area enhancement, the droplets coalesce into a single droplet. Under certain conditions, on the other hand, this impingement may cause the droplets to break into several smaller spherical droplets. Thus, even when the alloy is kept within the miscibility gap for long periods of time, there is an abundance of fine L1 spheres in the microstructure.

4. Summary

The microstructure of TIG and electron beam welding of copper/stainless-steel tubes was investigated, utilizing scanning electron microscopy. The following results were obtained:

1. The high cooling rates involved in TIG and electron beam welding induce high bulk supercooling of the liquid in the molten pool. This causes separation into two liquids: a Fe-rich liquid L1 and a Cu-rich liquid L2. Each of the liquids solidifies along a path dictated by the stable phase boundaries. The microstructure consisted of spherulites embedded in a matrix. The spherulites in alloys that contain up to 50 wt % Fe solidify from the L1 melt, while in alloys that contain more than 50 wt % Fe, spherulites solidify from the L2 melt.
2. Enhanced solute trapping of Fe in the ε-Cu was observed.

Acknowledgements

The author thanks C. Cotler, H. Sacham and M. Aberman for their technical assistance and Dr Z. Burshtein for his critical reading of the manuscript.

References

1. A. MUNITZ, *Metallurgical Transactions B* **18B** (1987) 565.
2. Z. LIVNE and A. MUNITZ, *J. Mater. Sci.* **22** (1987) 495.
3. S. P. ELDER, A. MUNITZ and R. ABBASCHIAN, *Materials Sci. Forum* **50** (1989) 137.
4. S. J. B. REED, "Electron microprobe analysis" (Cambridge University Press, Cambridge, 1977) pp. 175–97.
5. A. MUNITZ, R. ABBACHIAN, C. COTLER and C. SHACHAM, Unpublished work.
6. W. A. TILLER, K. A. JACKSON, J. W. RUTTER and B. CHALMERS, *Acta Metall.* **1** (1953) 428.
7. A. MUNITZ, S. ELDER and G. J. ABBASCHIAN, *Met. Trans. A.* **23A** (1992) 1817–27.
8. A. MUNITZ and R. ABBASCHIAN, Unpublished work.
9. I. S. MIROSHNICHENKO and G. P. BREKHARYA, *Fiz. Metal. Metalloved.* **20** (1970) 664.
10. T. R. ANTHONY and H. E. CLINE, *J. Appl. Phys.* **48** (1977) 3888.
11. R. R. SHAW and J. F. BREEDIS, *J. Am. Cer. Soc.* **55** (1972) 422–5.
12. W. VOGEL, "Chemistry of glass", edited and translated by N. Keridl (American Ceramic Society, Inc., Columbus, OH, 1985) pp. 86–8.
13. M. S. RANDALL, J. H. SIMMONS and O. H. EL-BAYOVMI, *J. Am. Ceram. Soc.* **71** (1988) 1134–41.

Received 9 November 1993
and accepted 17 August 1994